Research Article | Vol. 28, No. 17 / 17 August 2020 / Optics Express 24568

Optics EXPRESS

X-ray imaging of fast dynamics with single-pixel detector

O. SEFI,[1] Y. KLEIN,[1] E. STRIZHEVSKY,[1] I. P. DOLBNYA,[2] AND S. SHWARTZ[1,*]

[1] *Physics Department and Institute of Nanotechnology, Bar-Ilan University, Ramat Gan 52900, Israel*
[2] *Diamond Light Source Ltd., Harwell Science & Innovation Campus, Didcot, Oxfordshire OX11 0DE, UK*
[*] *sharon.shwartz@biu.ac.il*

Abstract: We demonstrate experimentally the ability to use a single-pixel detector for two-dimensional high-resolution x-ray imaging of fast dynamics. We image the rotation of a spinning chopper at 100 kHz and at spatial resolution of about 40 microns by using the computational ghost imaging approach. The technique we develop can be used for the imaging of fast dynamics of periodic and periodically stimulated effects with a large field of view and at low dose.

1. Introduction

X-ray imaging methods are used for numerous applications in a variety of areas ranging from basic science to medicine and security. The main advantage of x-rays for imaging is their unique capability to penetrate through surfaces, which are opaque to other commonly used wavelengths, such as visible and infrared. While most x-ray pixelated detectors are used for static applications, there is a growing need for detectors with combined high spatial resolution and at high frame rates. These detectors will open a new horizon for the application of x-rays for measurements of dynamics of systems, such as acoustic waves in matter, dynamics of phase transitions, and medical imaging. This innovative function will be essential for the understanding of numerous phenomena and processes and can lead to novel applications.

However, similar to detectors for other regimes of the electromagnetic spectrum, two-dimensional (2D) x-ray detectors are much slower than single-pixel detectors, while single-pixel detectors cannot provide the spatial resolution directly. Even with the improvements in detector technologies, the fundamental tradeoff between the number of pixels and the readout time is a major challenge. For example, for detectors with 1360×1080 pixels the frame rates are about 10 frames per second [1]. Other detectors with fewer pixels can be faster, but they exhibit either poor resolution or small field of views [2,3]. We note that modern detectors can use fast electronic shutters for short acquisition times on the order of only a few microseconds, but their frame rates, field of views and spatial resolution are still quite limited and they are very expensive [4,5]. While other x-ray cameras exhibit frame rates on the order of a few MHz, the number of recorded frames is limited [6]. Sophisticated imaging methods, such as pulse isolation and pump-probe imaging [7–10], have shown some success as well. However, those methods require very specific time structures of the sequence of synchrotron radiation pulses and can be performed only at a few dedicated beamlines, thus their availability is limited. Moreover, none of those methods can be performed with x-ray tubes, which are the most abundant x-ray sources.

A possible route for a novel imaging technique that offers high frame rate imaging at high resolution and that does not require special synchrotron beams and pulse structures can be based on the method of thermal (or pseudothermal) ghost imaging (GI) [11–13]. This is a lensless imaging technique, which uses the intensity fluctuations of the input beam. The intensity fluctuation can be added by various means such as natural fluctuations of thermal sources [14,15], spatial light modulators [16,17], mirrors [18], and diffusers [19–22]. In the traditional scheme [14,19,23,24], the beam is split into two portions with correlated intensity fluctuations patterns,

#396497
Journal © 2020

https://doi.org/10.1364/OE.396497
Received 4 May 2020; revised 5 Jul 2020; accepted 7 Jul 2020; published 5 Aug 2020

by a beam-splitter. A portion of the beam (usually about 50% of the intensity), which is called the reference beam, propagates freely and is collected by a two-dimensional detector that measures the spatial distribution of the intensity fluctuations. The second portion of the beam, which is called the test beam, impinges on the object. The beam can be either transmitted or reflected from the object and is collected by a single-pixel detector that measures only the total intensity. The image is reconstructed by correlating the reference and the test beams for many different realizations of illumination patterns. In another approach for the implementation of GI [17,20–22,25,26], the measurements are performed in two steps: first, the distributions of the intensity fluctuations for the various realizations are measured and recorded by the two-dimensional detector in the absence of the object. In the second step the object is inserted, the two-dimensional detector is replaced by a single-pixel detector, and the measurements of the test beam are recorded. After the two sets of measurements are completed, the image is reconstructed by correlating the measurements from each realization.

GI has been demonstrated mainly with optical sources [11,12,16,17,22,26] and recently with x-rays [14,19–21,23–25,27–29], atoms [30], electrons [31], and neutrons [32]. In addition, far field GI [21,33,34], GI in the time domain [35], ghost polarimetry [36], ghost tomography [24], and ghost spectroscopy [37] have been demonstrated as well.

In this work we demonstrate experimentally, for the first time, the possibility to use x-ray GI to image fast dynamics. We use the method to image the motion of a chopper spinning at 200 Hz, where the frame rate is 100 kHz and at spatial resolution of about 40 microns and with a field of view of 0.6 mm $\times$ 0.6 mm. The procedure we demonstrate can be used for the study of dynamics for a variety of phenomena with x-rays.

2. Experiment & procedure

While in the standard GI the object is static, the method can be extended for the imaging of periodically moving objects by using a procedure similar to the procedure shown by Zhao et al. with an optical source [16]. The schematic of the procedure is described in Fig. 1(a). First, the whole set of reference measurements is carried out by raster scanning a diffuser and recording the images by a slow pixilated detector with high spatial resolution. In the second step, we measure the test beam. This is done by measuring the intensity with a single-pixel detector at high sampling rates, for the entire period of the motion of the object for one position of the diffuser. Since this system measures only the signal of a single-pixel detector, the frequency of the recorded data can exceed tens of MHz. Each position of the diffuser produces a set of test signals, corresponding to different positions along the trajectory of the object. We repeat this measurement for the same set of realizations as was done with the reference beam by raster scanning the diffuser. Next, we reorder the recorded data sets to create a new sequence of data sets where each includes the measurements of the reference and the test beams for all the positions of the diffuser for one frame (one position of the object). We do that by using the information from the synchronization signal. We then corelate the reference and the test beams for each frame separately to reconstruct the image as is done with the static GI. In the final step, we construct the sequence of the frames by concatenating the individual frames.

We performed the experiment on the B16 beamline at the Diamond Light Source. The schematic description of the experimental setup is shown in Fig. 1(b)-(c). We exploit the two-step approach for the implementation of pseudothermal GI as we described above. We use a monochromatic beam at 9 keV on which we place a squared aperture with the size of 0.6 mm $\times$ 0.6 mm. The beam propagates through a sandpaper with an average feature size of about 10 µm, that we use as a diffuser, mounted on two-dimensional motorized stages, that we use for the introduction of the intensity fluctuations into the beam. We measure and record the intensity fluctuations with a Photonic Science X-ray MiniFDS camera for which the pixel size is 6.5 µm and the frame rate is 7.5 frames per second. An explanatory image of the reference beam can be

Optics EXPRESS

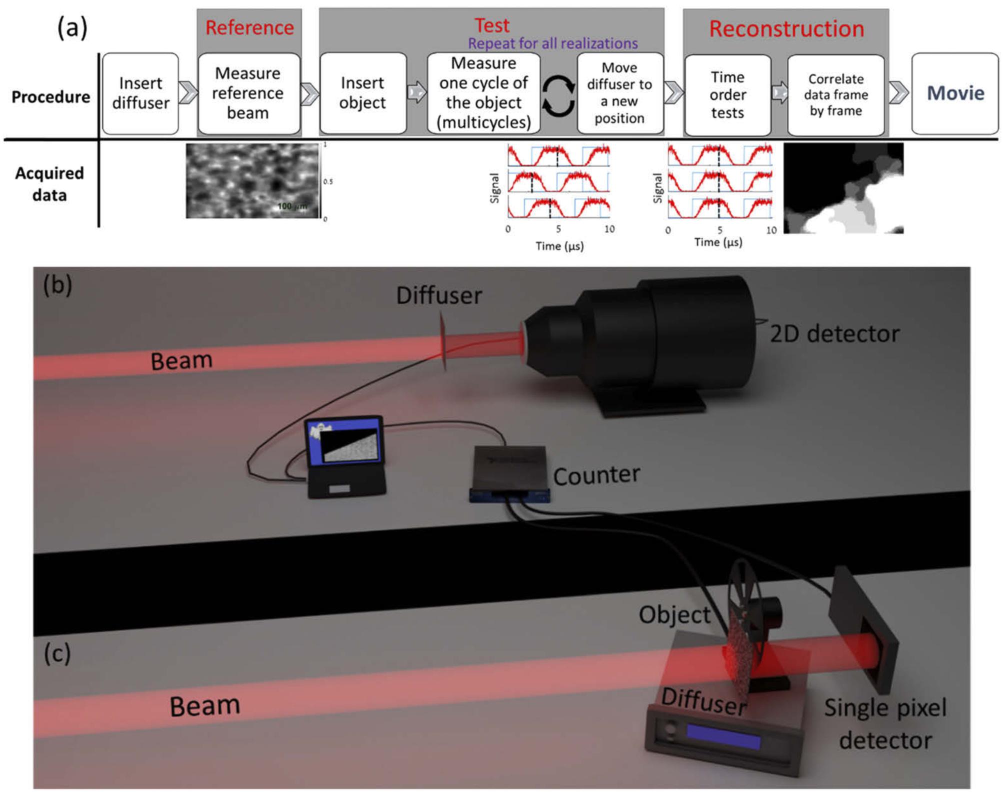

Fig. 1. (a) The measurement procedure. (b) The experimental setup for the reference beam measurements: The intensity fluctuations are introduced into the beam by a motorized diffuser. Afterwards, the intensity distribution is measured by a 2D x-ray detector. (c) The setup for the test beam measurements: The intensity fluctuations are introduced into the beam by the diffuser and the beam impinges on the object. The beam that is transmitted through the object is collected by a single-pixel detector.

seen in Fig. 1(a). We repeat the diffuser measurements several times to verify that the intensity fluctuation patterns are stable against fluctuations in the beam and mechanical shifts. After we measure the diffuser, we insert the object, an optical chopper rotating at chopping frequency of 200 Hz with jitter of 0.2 deg per cycle. The velocity of the blades of the chopper is about 0.6 m/sec. We use the chopper output signal for synchronization. For the measurements of the test beam we use an avalanche photodiode detector (APD). We record the data with a NI-DAQ USB X SERIES data acquisition card at the sampling rate of 100 kHz. An example for the test and for the chopper signals can be seen in Fig. 1(a).

In order to reduce the number of required realizations we use the compressive sensing approach, which uses a prior information on the structure of the image. We implement this approach by the TVAL3 reconstruction algorithm [17,38,39]. The basic idea is to recognize that the gradient of many objects in nature can be represented by a sparse matrix. One can reconstruct the image u of such an object by minimizing the augmented Lagrangian:

$$\min_{u} \Sigma_i ||D_i u||_2 + \frac{\mu}{2} ||Au - b||_2^2 \ , \ s.t. \ \ u \geq 0$$

here, $||\cdot||_2$ is the L_2 norm, $D_i u$ is the i$^{\text{th}}$ component of the discreet gradient of the image u, and μ is the penalty parameter of the model (here we set $\mu = 2^8$). A and b are the reference and test

Optics EXPRESS

measurements respectively. As a consequence of this condition the algorithm favors images, for which the L_2 norm of the gradient is minimal.

3. Results & discussion

We start by showing several snapshots from the reconstructed movie of the optical chopper in Fig. 2. The number of pixels in each frame is 8550 and the frame rate is 10^5 frames per second. In each test realization we sum over 400 periods of the chopper to enhance the test signal and improve the signal-to-noise ratio (SNR). We use 4900 realizations per each frame with an average of $8.5 \cdot 10^3$ counts per realization. In the upper left frame, the blade of the chopper blocks almost the entire beam except from a small area near the bottom right corner. The next panel shows the 6^{th} later frame where the chopper blocks a smaller portion of the beam. The rest of the frames show the motion of the chopper at measurement times that are indicated in the figure until the bottom right panel where the blade blocks the beam except from a small area near the upper left corner. The corresponding movie is provided in Visualization 1.

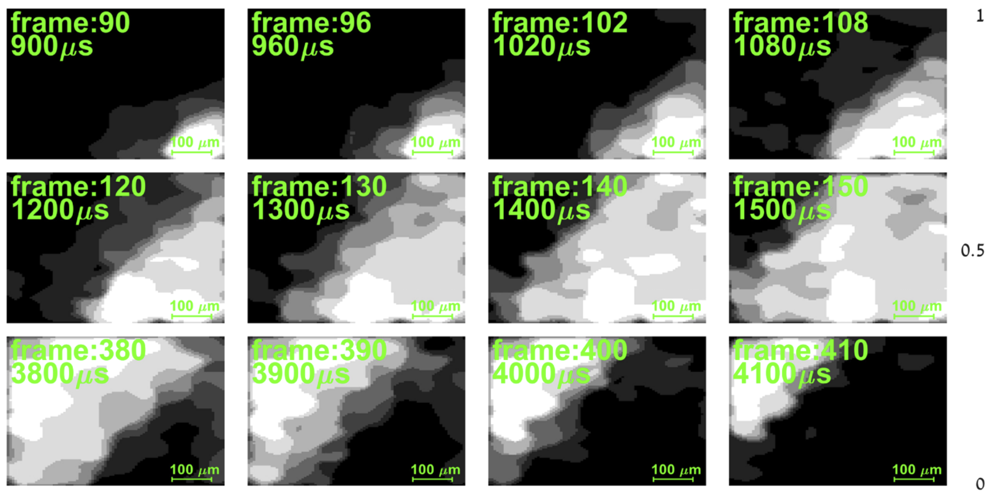

Fig. 2. Reconstructed movie frames of an optical chopper rotating at 200 Hz. The movie is recorded at a frame rate of 10^5 frames per second (see Visualization 1). The average flux in each test measurement is $\sim 8.5 \cdot 10^3$ counts. Each frame has $\sim 8.5 \cdot 10^3$ pixels with pixel size of 6.5 microns. The intensities of the images are normalized, see details in the text.

Note that the edge of the blade shown in the images is smeared over a distance of about 50 microns. There are several reasons for that blurring: 1. Since we average over multicycles, the jitter of the chopper, which is about 0.2 deg per one blade cycle, is responsible for smearing of 10 microns. 2. The resolution of the x-ray two-dimensional detector we used for the reference beam leads to additional blurring of about 25 microns. 3. We believe that remaining blurring, of about 15 microns, is originated from the reconstruction algorithm. The distance that the blades move during one single-pixel detector measurement (10 µs) is about 6 microns and therefore negligible. Usage of an algorithm, which is tailored to fit the system requirements is likely to improve the resolution of the system. Additionally, usage of a fabricated diffuser with smaller features while replacing the pixelated detector with propagation calculations, such as in computational GI, can improve the resolution further [20].

After demonstrating the feasibility of x-ray imaging of fast dynamics, we explore the quality of the reconstruction and its dependence on the number of realizations. We show the dependence of the SNR on the number of realizations in Fig. 3. The blue dots are the SNR that is calculated from the measured data and the red solid line is the fitting function $f = a\sqrt{N}$ with $a = 0.1033$.

Here, we use the standard definition of $SNR = \mu_I/\sigma_I$, where I is a vector of the intensities of several pixels in the illuminated area of the image, μ_I is the ensemble average, and σ_I is the standard deviation. The errors associated with the SNR are estimated by the standard error of the SNR, namely $\left(1/I + \mu^2/\sigma^3\sqrt{I}\right)^{1/2}$, and assuming Poissonian statistics. The largest vertical error is about 10^{-4}. Theoretically, the SNR of standard GI scales as the squared root of the number of realizations divided by the number of spatial resolution-cells in the image p, namely: $SNR \propto \sqrt{N/p}$ [28,40]. We note, that with partially coherent source and amplitude diffuser as in the case of the present experiment, the area of the resolution-cell is defined by the average feature size of the diffuser [40]. Since in our procedure we use the compressive sensing approach, the SNR is large by about an order of magnitude for the same number of realizations N [17].

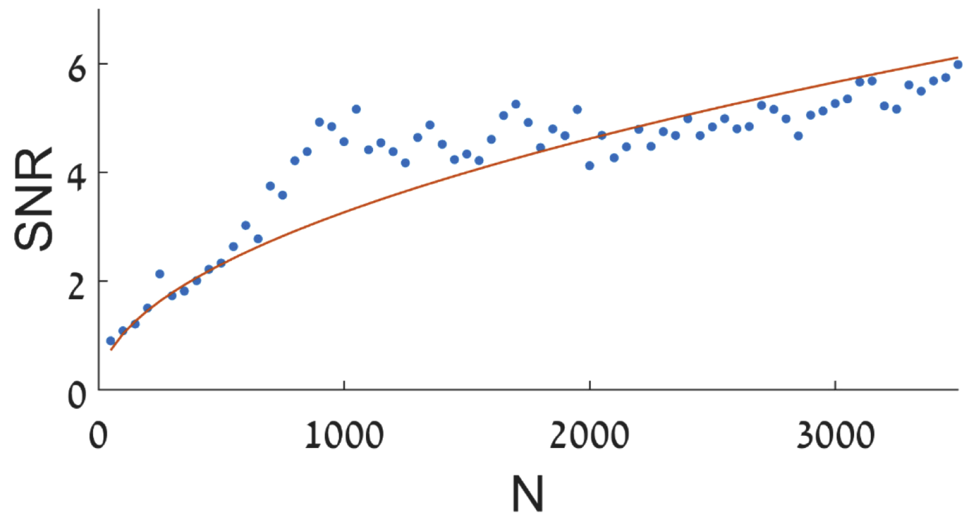

Fig. 3. The SNR as a function of the number of realizations N for frame 112 of the movie. The blue dots are experimental results and the red solid line is the analytical fitting function $a\sqrt{N}$. The largest vertical error associated with the SNR is about 10^{-4}. See details in the text.

Low dose imaging

One of the main potential advantages of GI is the opportunity for low dose imaging [14,25,28,41]. We explore this possibility by investigating the dependence of the SNR on the number of the photons detected by the test detector. Here, instead of summing over the whole 400 cycles of the chopper, which we recorded, we use a smaller number of cycles, varying from single cycle to 50 cycles. Consequently, the radiation dose impinge on the object is smaller. The results are summarized in Fig. 4(a) where the dependence of the SNR on the number of detected photons is shown. Here, the blue dots indicate the SNR calculated from the measured data and the error bars indicate the counting statistics. The SNR and its error are calculated as in Fig. 3. The insets (b)-(d) are the corresponding reconstructed images for 30, 375, and 1160 counts at the single-pixel detector.

The dependence of the SNR on the number of photons can be separated into two distinct regions. In the low flux region (up to about 200 counts) the SNR scales as $a\sqrt{N}$ with $a = 0.055$, like the dependence shown in Fig. 3. However, at higher flux the dependence on the number of photons is weaker. In this region the coefficient a is reduced by about factor of 5. This dependence indicates that in the high flux regime the statistical error is negligible and other

Optics EXPRESS

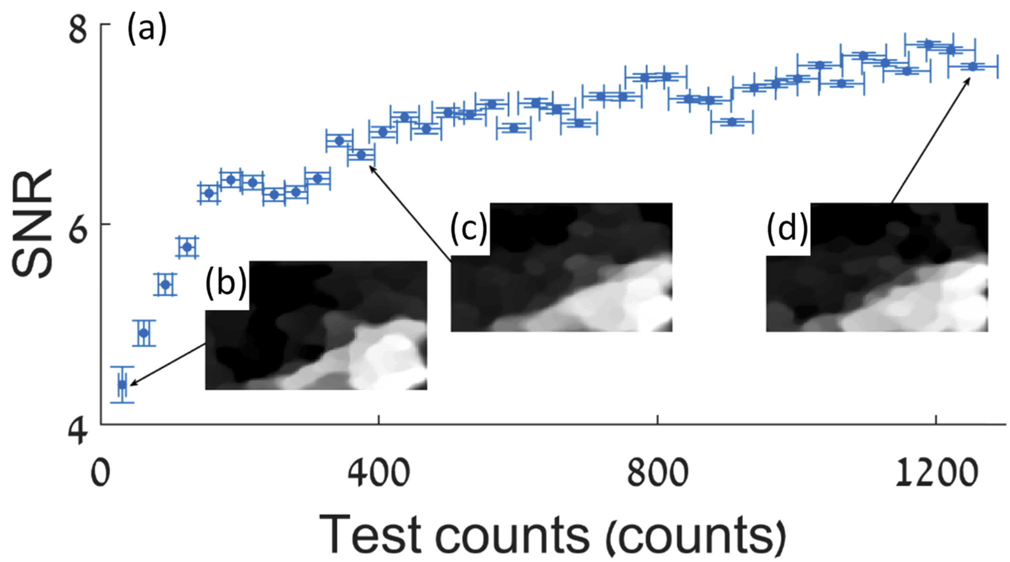

Fig. 4. (a) Dependence of the SNR on the flux of the test beam corresponding to frame 112 in the movie. The horizontal error bars indicate the counting statistics. In the insets (b-d) we show the reconstructed images corresponding to 30, 375, and 1160 counts at the detector, respectively.

sources for noise, that probably can be reduced, dominate the noise in this regime. In the low dose region however the main source of noise is shot noise, which is standard quantum limit and it is the lowest achievable noise with classical sources.

We further illustrate the low dose imaging capabilities by showing snapshots from the reconstructed movie under low dose conditions in Fig. 5. Here, we use a single cycle of the motion of the chopper per test measurement. Consequently, the number of photons impinge on the object during one single-pixel measurement is about 50. We use 4900 realizations and reconstruct images, which include 8500 pixels and measure on average about 30 counts per frame per pixel. The frames that we show here are the same as in Fig. 2 and they describe the same dynamics. This result shows the feasibility to retrieve reasonable results even with extremely small amount of radiation, which is orders of magnitude smaller than the radiation levels used in traditional direct imaging. This capability is extremely important for imaging of fast processes, where the exposure times are inherently short thus associated with a small number of photons per frame. The corresponding movie is provided in Visualization 2.

Before concluding, we discuss two important aspects related to the spatial and temporal resolution of the system. Of importance, the spatial resolution is determined by the resolution of the measurements of the reference beam. Here, we used an x-ray pixilated detector with a limited resolution to perform those measurements. It is possible to improve the resolution by using a free-propagation calculation from a diffuser with known smaller features that can be fabricated with nanotechnology techniques, as is done in computational GI [20,22]. As for the temporal resolution, in our system the frame rate was limited by the DAQ sampling frequency. However faster DAQs are available, with sampling frequencies up to 100 MHz. The next factor, which limits the frame rate is the detection time of the APD, which is about 10 ns for standard APDs. It is worth mentioning that while the characterization of the diffuser is time consuming (several seconds per realization), once it is done, the same diffuser can be used for the reconstruction of unlimited number of objects. The test measurements can be done at much faster rates and are currently limited by the speed of the motors on which the diffuser is mounted.

Optics EXPRESS

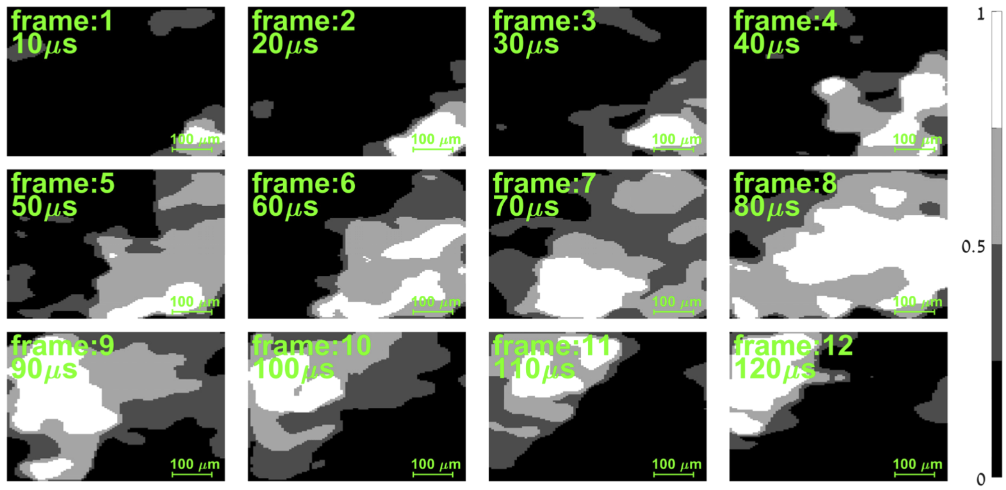

Fig. 5. Low-dose reconstructed movie frames of an optical chopper rotating at 200 Hz (see Visualization 2). The average number of photons in each test measurement is 24. Each frame includes ~$8.5 \cdot 10^3$ pixels with pixel size of 6.5 microns. The intensities are normalized, see details in the text.

4. Conclusions

We have demonstrated the ability to use the method of GI for high-resolution large field of view x-ray imaging of fast dynamics. We have also shown that the method can be used for low dose imaging. The procedure and results we have described open new possibilities for the study of fast dynamics of processes, which can be triggered periodically and can be synchronized. The method is not limited to transmission measurements and can be used for phase contrast measurements [29,42] and for incoherent diffraction imaging [21,29]. Finally, we note that in contrast to other available x-ray imaging techniques for fast dynamics, our method can be implemented with conventional x-ray tubes. Hence it can be applied for medical imaging where measurements of fast dynamics are required, for example for non-invasive cardiac imaging, and for non-destructive imaging of moving mechanical components.

Funding

EU Framework Program for Research and Innovation Horizon 2020 Framework Programme (CALIPSOplus 730872).

Acknowledgments

We thank Diamond Light Source for access to Beamline B16 (Proposal No. MM23604), which contributed to the results presented here.

Disclosures

The authors declare no conflicts of interest.

References

1. J.-C. Labiche, O. Mathon, S. Pascarelli, M. A. Newton, G. G. Ferre, C. Curfs, G. Vaughan, A. Homs, and D. F. Carreiras, "Invited article: The fast readout low noise camera as a versatile x-ray detector for time resolved dispersive extended x-ray absorption fine structure and diffraction studies of dynamic problems in materials science, chemistry, and catalysis," Rev. Sci. Instrum. **78**(9), 091301 (2007).

2. I. Ordavo, S. Ihle, V. Arkadiev, O. Scharf, H. Soltau, A. Bjeoumikhov, S. Bjeoumikhova, G. Buzanich, R. Gubzhokov, A. Günther, R. Hartmann, P. Holl, N. Kimmel, M. Kühbacher, M. Lang, N. Langhoff, A. Liebel, M. Radtke, U. Reinholz, H. Riesemeier, G. Schaller, F. Schopper, L. Strüder, C. Thamm, and R. Wedell, "A new pnCCD-based color X-ray camera for fast spatial and energy-resolved measurements," Nucl. Instrum. Methods Phys. Res., Sect. A **654**(1), 250–257 (2011).
3. A. Rack, M. Scheel, and A. N. Danilewsky, "Real-time direct and diffraction X-ray imaging of irregular silicon wafer breakage," IUCrJ **3**(2), 108–114 (2016).
4. H. T. Philipp, M. W. Tate, P. Purohit, K. S. Shanks, J. T. Weiss, and S. M. Gruner, "High-speed X-ray imaging pixel array detector for synchrotron bunch isolation," J. Synchrotron Radiat. **23**(2), 395–403 (2016).
5. B. R. Halls, C. D. Radke, B. J. Reuter, A. L. Kastengren, J. R. Gord, and T. R. Meyer, "High-speed, two-dimensional synchrotron white-beam x-ray radiography of spray breakup and atomization," Opt. Express **25**(2), 1605 (2017).
6. M. P. Olbinado, X. Just, J.-L. Gelet, P. Lhuissier, M. Scheel, P. Vagovic, T. Sato, R. Graceffa, J. Schulz, A. Mancuso, J. Morse, and A. Rack, "MHz frame rate hard X-ray phase-contrast imaging using synchrotron radiation," Opt. Express **25**(12), 13857 (2017).
7. J. S. Lee, B. M. Weon, S. J. Park, J. H. Je, K. Fezzaa, and W.-K. Lee, "Size limits the formation of liquid jets during bubble bursting," Nat. Commun. **2**(1), 367 (2011).
8. Y. Wang, X. Liu, K.-S. Im, W.-K. Lee, J. Wang, K. Fezzaa, D. L. S. Hung, and J. R. Winkelman, "Ultrafast X-ray study of dense-liquid-jet flow dynamics using structure-tracking velocimetry," Nat. Phys. **4**(4), 305–309 (2008).
9. M. Cammarata, L. Eybert, F. Ewald, W. Reichenbach, M. Wulff, P. Anfinrud, F. Schotte, A. Plech, Q. Kong, M. Lorenc, B. Lindenau, J. Räbiger, and S. Polachowski, "Chopper system for time resolved experiments with synchrotron radiation," Rev. Sci. Instrum. **80**(1), 015101 (2009).
10. H. S. Cho, N. Dashdorj, F. Schotte, T. Graber, R. Henning, and P. Anfinrud, "Protein structural dynamics in solution unveiled via 100-ps time-resolved x-ray scattering," Proc. Natl. Acad. Sci. **107**(16), 7281–7286 (2010).
11. F. Ferri, D. Magatti, A. Gatti, M. Bache, E. Brambilla, and L. A. Lugiato, "High-Resolution Ghost Image and Ghost Diffraction Experiments with Thermal Light," Phys. Rev. Lett. **94**(18), 183602 (2005).
12. A. Valencia, G. Scarcelli, M. D'Angelo, and Y. Shih, "Two-Photon Imaging with Thermal Light," Phys. Rev. Lett. **94**(6), 063601 (2005).
13. R. S. Bennink, S. J. Bentley, and R. W. Boyd, ""Two-Photon" Coincidence Imaging with a Classical Source," Phys. Rev. Lett. **89**(11), 113601 (2002).
14. D. Pelliccia, A. Rack, M. Scheel, V. Cantelli, and D. M. Paganin, "Experimental X-Ray Ghost Imaging," Phys. Rev. Lett. **117**(11), 113902 (2016).
15. G. Scarcelli, V. Berardi, and Y. Shih, "Can Two-Photon Correlation of Chaotic Light Be Considered as Correlation of Intensity Fluctuations?" Phys. Rev. Lett. **96**(6), 063602 (2006).
16. W. Zhao, H. Chen, Y. Yuan, H. Zheng, J. Liu, Z. Xu, and Y. Zhou, "Ultrahigh-Speed Color Imaging with Single-Pixel Detectors at Low Light Level," Phys. Rev. Appl. **12**(3), 034049 (2019).
17. O. Katz, Y. Bromberg, and Y. Silberberg, "Compressive ghost imaging," Appl. Phys. Lett. **95**(13), 131110 (2009).
18. Y. Wang, Y. Liu, J. Suo, G. Situ, C. Qiao, and Q. Dai, "High Speed Computational Ghost Imaging via Spatial Sweeping," Sci. Rep. **7**(1), 45325 (2017).
19. A. Schori and S. Shwartz, "X-ray ghost imaging with a laboratory source," Opt. Express **25**(13), 14822 (2017).
20. Y. Klein, A. Schori, I. P. Dolbnya, K. Sawhney, and S. Shwartz, "X-ray computational ghost imaging with single-pixel detector," Opt. Express **27**(3), 3284 (2019).
21. H. Yu, R. Lu, S. Han, H. Xie, G. Du, T. Xiao, and D. Zhu, "Fourier-Transform Ghost Imaging with Hard X Rays," Phys. Rev. Lett. **117**(11), 113901 (2016).
22. J. H. Shapiro, "Computational ghost imaging," Phys. Rev. A **78**(6), 061802 (2008).
23. A. Schori, D. Borodin, K. Tamasaku, and S. Shwartz, "Ghost imaging with paired x-ray photons," Phys. Rev. A **97**(6), 063804 (2018).
24. A. M. Kingston, D. Pelliccia, A. Rack, M. P. Olbinado, Y. Cheng, G. R. Myers, and D. M. Paganin, "Ghost tomography," Optica **5**(12), 1516 (2018).
25. A.-X. Zhang, Y.-H. He, L.-A. Wu, L.-M. Chen, and B.-B. Wang, "Tabletop x-ray ghost imaging with ultra-low radiation," Optica **5**(4), 374 (2018).
26. Y. Bromberg, O. Katz, and Y. Silberberg, "Ghost imaging with a single detector," Phys. Rev. A **79**(5), 053840 (2009).
27. D. Pelliccia, M. P. Olbinado, A. Rack, A. M. Kingston, G. R. Myers, and D. M. Paganin, "Towards a practical implementation of X-ray ghost imaging with synchrotron light," IUCrJ **5**(4), 428–438 (2018).
28. D. Ceddia and D. M. Paganin, "Random-matrix bases, ghost imaging, and x-ray phase contrast computational ghost imaging," Phys. Rev. A **97**(6), 062119 (2018).
29. M. P. Olbinado, D. M. Paganin, Y. Cheng, and A. Rack, "Phase-sensitive x-ray ghost imaging," arXiv Prepr. arXiv1903.08345 (2019).
30. R. I. Khakimov, B. M. Henson, D. K. Shin, S. S. Hodgman, R. G. Dall, K. G. H. Baldwin, and A. G. Truscott, "Ghost imaging with atoms," Nature **540**(7631), 100–103 (2016).
31. S. Li, F. Cropp, K. Kabra, T. J. Lane, G. Wetzstein, P. Musumeci, and D. Ratner, "Electron Ghost Imaging," Phys. Rev. Lett. **121**(11), 114801 (2018).
32. A. M. Kingston, G. R. Myers, D. Pelliccia, F. Salvemini, J. J. Bevitt, U. Garbe, and D. M. Paganin, "Neutron ghost imaging," Phys. Rev. A **101**(5), 053844 (2020).

Optics EXPRESS

33. H. Liu, X. Shen, D.-M. Zhu, and S. Han, "Fourier-transform ghost imaging with pure far-field correlated thermal light," Phys. Rev. A **76**(5), 053808 (2007).
34. M. Zhang, Q. Wei, X. Shen, Y. Liu, H. Liu, J. Cheng, and S. Han, "Lensless Fourier-transform ghost imaging with classical incoherent light," Phys. Rev. A **75**(2), 021803 (2007).
35. P. Ryczkowski, M. Barbier, A. T. Friberg, J. M. Dudley, and G. Genty, "Ghost imaging in the time domain," Nat. Photonics **10**(3), 167–170 (2016).
36. P. Janassek, S. Blumenstein, and W. Elsäßer, "Recovering a hidden polarization by ghost polarimetry," Opt. Lett. **43**(4), 883 (2018).
37. P. Janassek, S. Blumenstein, and W. Elsäßer, "Ghost Spectroscopy with Classical Thermal Light Emitted by a Superluminescent Diode," Phys. Rev. Appl. **9**(2), 021001 (2018).
38. Y. Sher, "Review of Algorithms for Compressive Sensing of Images," arXiv prepr. arXiv:1908.01642 (2019).
39. C. Li, W. Yin, H. Jiang, and Y. Zhang, "An efficient augmented Lagrangian method with applications to total variation minimization," Comput. Optim. Appl. **56**(3), 507–530 (2013).
40. B. I. Erkmen and J. H. Shapiro, "Signal-to-noise ratio of Gaussian-state ghost imaging," Phys. Rev. A - At. Mol. Opt. Phys. (2009).
41. T. J. Lane and D. Ratner, "What are the advantages of ghost imaging? Multiplexing for x-ray and electron imaging," Opt. Express **28**(5), 5898 (2020).
42. T. Shirai, T. Setälä, and A. T. Friberg, "Ghost imaging of phase objects with classical incoherent light," Phys. Rev. A **84**(4), 041801 (2011).